mathematics

MDPI

Article

Smoothing Filter and Correction Factor for Two-Dimensional Electrical Resistivity Tomography and Time Domain-Induced Polarization Data Collected in Difficult Terrains to Improve Inversion Models

Andrés Tejero-Andrade [1,*], Aide E. López-González [1], José M. Tejero-Andrade [2], René E. Chávez-Segura [3] and Denisse L. Argote [4]

[1] Facultad de Ingeniería de la UNAM, Universidad Nacional Autónoma de México, Avenida Universidad 3000, Ciudad Universitaria, Mexico City 04510, Mexico; aide.lopez@ingenieria.unam.edu
[2] Department Metal-Mechanics, Tecnológico Nacional de México, Campus Veracruz, Calz, Miguel Ángel de Quevedo 2779 Veracruz, Veracruz 91897, Mexico
[3] Instituto de Geofísica de la Universidad Nacional Autónoma de México, Circuito de la Investigación Científica s/n, Ciudad Universitaria, Mexico City 04510, Mexico
[4] Dirección de Estudios Arqueológicos, Instituto Nacional de Antropología e Historia, Licenciado Primo de Verdad 3, Colonia Centro, Mexico City 06060, Mexico; denisse_argote@inah.gob.mx
* Correspondence: atatejero16@gmail.com

check for updates

Academic Editor: Maria C. Mariani

Received: 21 January 2025
Revised: 28 February 2025
Accepted: 2 March 2025
Published: 5 March 2025

Citation: Tejero-Andrade, A.; López-González, A.E.; Tejero-Andrade, J.M.; Chávez-Segura, R.E.; Argote, D.L. Smoothing Filter and Correction Factor for Two-Dimensional Electrical Resistivity Tomography and Time Domain-Induced Polarization Data Collected in Difficult Terrains to Improve Inversion Models. *Mathematics* **2025**, *13*, 866. https://doi.org/10.3390/math13050866

Correction Statement: This article has been republished with a minor change. The change does not affect the scientific content of the article and further details are available within the backmatter of the website version of this article.

Copyright: © 2025 by the authors. Licensee MDPI, Basel, Switzerland. This article is an open access article distributed under the terms and conditions of the Creative Commons Attribution (CC BY) license (https://creativecommons.org/licenses/by/4.0/).

Abstract: When collecting data using ERT2D (2D electrical resistivity tomography) and TDIPT2D (2D time domain-induced polarization), different phenomena can occur, which can cause natural or anthropogenic noise, contaminating the data and making its processing, analysis, and interpretation difficult. Different techniques have been developed to eliminate or reduce these effects on the data, such as noise filtering or the development of new techniques to improve data collection in the field. In the present work, an iterative, weighted, least-squares filter was employed after voltage normalization using current and geometrical factor correction on data collected in rough topographic terrains. The selected filter basis function should be able to represent the natural behavior of the function to be filtered. Stationary or variable voltages in electrical prospecting decay with the inverse of the distance, which can be represented by an expansion in Legendre polynomials. On the other hand, uneven spacing of the electrodes leads to using the incorrect geometric factor, resulting in an error in the calculation of the electrical anomaly. The efficiency of the proposed technique was analyzed and tested with field examples using different filters and by comparing applying and not applying the proposed correction factor. The results indicated low RMS and L2-Norm errors, and better definition of the inverted resistivity image was obtained. For the TDIP data, a better correspondence between the inverted images of resistivity and chargeability was obtained.

Keywords: smoothing filter; Legendre polynomials; ERT2D; TDIP2D; topographical effects; improving inversion

MSC: 86A20

1. Introduction

In recent years, 2D electrical resistivity tomography (ERT2D) and time domain-induced polarization (TDIP2D) have been proven to be efficient methods for addressing problems in near-surface geophysics. These methods have been particularly useful in civil and

geotechnical engineering [1,2], archeology [3], hydrogeophysics [4], and studying soil contamination [5], fracture flow paths [6], and dynamic processes such as water movement in vadose zones [7]. They have also been used to study steam injection [8], air spray [9], and contaminant transport [10], and in emerging areas such as agriculture [11] and forensic research [12,13].

Despite their widespread application, ERT2D and TDIP2D are often affected by noise, particularly in urban or contaminated areas, such as those polluted with hydrocarbons. In many cases, significant amounts of noisy data must be discarded to improve the inversion models, which can reduce the resolution. Therefore, it is essential to develop new data collection techniques and efficient filters to minimize or remove random noise to allow the computation inversion process to produce more accurate and reliable inversion models.

Noise in ERT data can lead to inaccurate inversion results or artifacts in the models [14]. This noise can be categorized as either systematic or random. Systematic noise includes electrode noise [15,16], cultural or anthropogenic noise [17], and noise introduced by low-pass filters in TDIP instruments, which affects early-time decay measurements [18], and from inductive coupling [19]. Although systematic noise is not the focus of this study, it is important to mention that it can be mitigated through improved data acquisition procedures, such as nighttime measurements, techniques to reduce contact resistance noise, and the development of new electrode arrays for specific objectives as second potential-difference measurements [20,21].

Random noise (RN) is the subject of this study. Traditionally, RN in ERT surveys has been addressed using smoothing filters [22], sliding or median averages [23], and de-spiking filters. Smoothing filters, such as least-squares filters, have been widely used with polynomial functions [17,24,25] or other methods [26] to reduce the effects of near-surface inhomogeneities that distort apparent resistivity pseudo-sections. However, these studies did not explore alternative basis functions for the polynomials, which this work does.

Other approaches to reduce RN include filters based on direct and reciprocal measurements [27] and wavelet-based filters, which were applied to well-log [28], DC resistivity [29], and TDIP data [30].

For geophysicists working in the frequency domain, it is known that there is limited literature on filtering time domain IP2D data due to the limited amount of discrete data available. Filtering TDIP frequency data depends on the equipment's capabilities and the number of samples it can acquire. It also requires a regular lattice in both the horizontal and vertical directions. More recently, full-waveform acquisition has been explored for noise suppression in TDIP data [17,31], which also requires smoothing and low-pass filters.

Wavelet and frequency filter processes have demonstrated good results; however, their application requires experience, time, and careful evaluation to decide where to cut signals.

Although other inversion methods have been developed, the most widely used ERT2D inversion approach remains the least-squares method. This method requires topographical corrections to reduce false anomalies. Additionally, smoothed data are needed to reduce root-mean-square (RMS) errors and to ensure that the data converge well during modeling (L2-Norm < 1.0%). In practice, geometrical factor errors often arise due to inaccurate electrode spacing. Furthermore, an irregular topography can alter anomalies, as some software transforms topography into a flat plane before inversion rather than considering inversion with the terrain profile. Finally, field voltages are measured using different DC current values injected into the subsoil. Even though these voltages are normalized by their corresponding current during inversion, errors can occur because the entire dataset is not standardized under the same current.

In TDIP, chargeability is generally not filtered, as it is considered a normalized parameter [32]. However, during the inversion process, the inverted chargeability model is derived

from the inverted conductivity model [33]. Thus, any normalization correction or filtering applied to the resistivity or conductivity data will inherently affect the chargeability.

This study aimed to develop improved smoothing filters for practitioners who frequently use ERT2D and TDIP and require enhanced signal clarity and reduced processing times. The proposed method involves three steps: voltage normalization, geometrical factor corrections, and an adaptive least-squares filter based on a fourth-degree Legendre polynomial (LSFLP) and a seven-sample window. This filter effectively removes random noise under the condition of equal sampling intervals and can be applied to resistivity and chargeability data.

The LSFLP can be applied independently, but when combined with voltage normalization and geometrical factor corrections, the resulting inversion models display better-defined anomalies without requiring increased smoothing or damping factors to reduce RMS and L2-Norm errors to below 1.0%.

Unfiltered data and data filtered using the LSFLP, a three-point moving average filter (MA), and a least-squares polynomial filter (Savitzky–Golay filter) were compared to test the performance of voltage normalization, geometrical factor corrections, and the different filters on two different ERT2D field datasets. The results highlight the improvements in identifying small resistivity and chargeability anomalies using the LSFLP.

2. Materials and Methods

The main issue is obtaining a numerical filter that is capable of eliminating or attenuating the effects of RN without altering or modifying the true pattern of the data. In this study, we designed a least-squares weighted filter (LSF) [34] with Legendre polynomials as the basis function (LSFLP) to process the data and compared it with other well-known filtering processes: a three-point moving average filter (MA) and Savitzky–Golay filter (Python library SciPy; modules scipy.signal and savgol-filter, using the same x, *window_length*, and *polyorder* as the LSFLP, which were iteratively applied 3 times). These three filtering methods were applied to each ERT2D and TDIP2D dataset level by level.

2.1. Smoothing Filter

An iterative least-squares smoothing method can be applied to efficiently smooth the original data. Such a filter ($\boldsymbol{F}$ in Equation (1)) can be defined by a Legendre polynomial function of the 4th degree, employing a window of 7 samples, and normalized by a rank of $[-1, 1]$ (LSFLP).

$$F = \sum_{i=-3}^{i=3} \sum_{l=0}^{l=4} a_{l,i} P_l\left(\frac{i}{3}\right). \tag{1}$$

where $P_l\left(\frac{i}{3}\right)$ are Legendre polynomials and $a_{l,i}$ are polynomial coefficients.

An LSF considers equally spaced samples and the smoothed filtered sample $\boldsymbol{s}_j$ is computed using Equation (2), written as follows:

$$s_j = \sum_{i=-3}^{i=3} y_{j+i} \sum_{l=0}^{l=4} a_{l,i} P_l\left(\frac{i}{3}\right). \tag{2}$$

where j = 4, 5, 6, $\cdots$, N $-$ 3, where N is the number of data points to be filtered.

However, interpolation can be carried out to avoid losing the first and last three data points using Equation (3), written as follows:

$$s_{3-k} = \textstyle\sum_{i=-3}^{i=3} y_{4+\mathrm{i}} \sum_{l=0}^{l=4} a_{l,i} P_l(i/3), \tag{3a}$$

$$s_{N-k} = \sum_{i=-3}^{i=3} y_{N-3+i} \sum_{l=0}^{l=4} a_{l,i} P_l(i/3). \quad k = 2, 1, 0. \tag{3b}$$

The sum of the coefficients (Equation (4)) must be equal to one.

$$\sum_{i=-3}^{i=3} \sum_{l=0}^{l=4} a_{l,i} = 1. \tag{4}$$

Figure 1 depicts the application of the filter to a noisy voltage signal from the archaeological zone of Mitla.

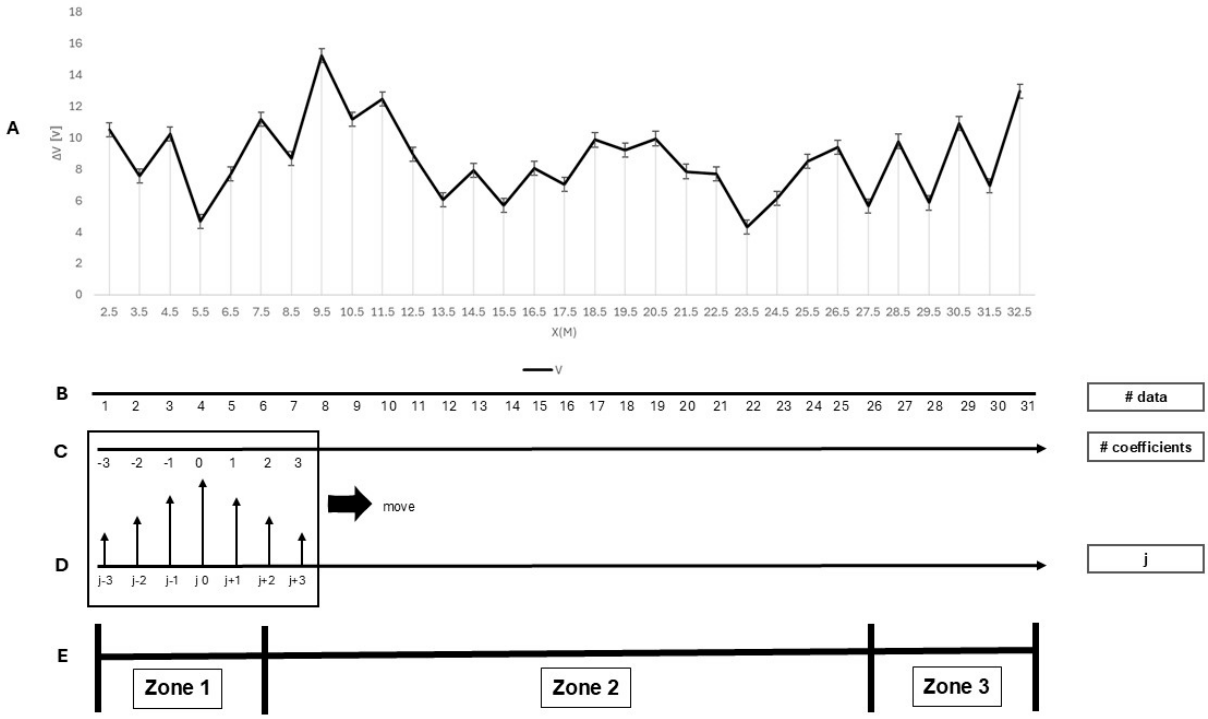


Figure 1. Data profile with the same spacing in the x-direction (**A**). A number of coefficients is assigned to each data point (**B**). The number of profile data points is indicated (**D**). For each number of coefficients, a data point P_l is obtained (**C**). The filter window moves from the first to the nth data point. The calculation of s_j will depend on the zone it is in (**E**).

2.2. Coefficient Calculation

From Equation (1), it follows that the coefficients $a_{l,i}$ have 7 values, one for each value of the 7-sample window. However, the solution of the equations to find the coefficients will be considered as a single value of $a_{l,i}$ to make the writing more concise. At the end, when the equations have been established, how each value for $a_{l,i}$ was deduced will be explained.

$$\begin{array}{c}
a_0P_0\left(-\frac{3}{3}\right) + a_1P_1\left(-\frac{3}{3}\right) + a_2P_2\left(-\frac{3}{3}\right) + a_3P_3\left(-\frac{3}{3}\right) + a_4P_4\left(-\frac{3}{3}\right) = 1 \\
a_0P_0\left(-\frac{2}{3}\right) + a_1P_1\left(-\frac{2}{3}\right) + a_2P_2\left(-\frac{2}{3}\right) + a_3P_3\left(-\frac{2}{3}\right) + a_4P_4\left(-\frac{2}{3}\right) = 1 \\
a_0P_0\left(-\frac{1}{3}\right) + a_1P_1\left(-\frac{1}{3}\right) + a_2P_2\left(-\frac{1}{3}\right) + a_3P_3\left(-\frac{1}{3}\right) + a_4P_4\left(-\frac{1}{3}\right) = 1 \\
a_0P_0\left(\frac{0}{3}\right) + a_1P_1\left(\frac{0}{3}\right) + a_2P_2\left(\frac{0}{3}\right) + a_3P_3\left(\frac{0}{3}\right) + a_4P_4\left(\frac{0}{3}\right) = 1 \\
a_0P_0\left(+\frac{1}{3}\right) + a_1P_1\left(+\frac{1}{3}\right) + a_2P_2\left(+\frac{1}{3}\right) + a_3P_3\left(+\frac{1}{3}\right) + a_4P_4\left(+\frac{1}{3}\right) = 1 \\
a_0P_0\left(+\frac{2}{3}\right) + a_1P_1\left(+\frac{2}{3}\right) + a_2P_2\left(+\frac{2}{3}\right) + a_3P_3\left(+\frac{2}{3}\right) + a_4P_4\left(+\frac{2}{3}\right) = 1 \\
a_0P_0\left(+\frac{1}{3}\right) + a_1P_1\left(+\frac{1}{3}\right) + a_2P_2\left(+\frac{1}{3}\right) + a_3P_3\left(+\frac{1}{3}\right) + a_4P_4\left(+\frac{1}{3}\right) = 1.
\end{array} \tag{5}$$

Equation (5) is written in matrix notation as $Pa = I$ (Equation (6)), where P is a 7-row × 5-column matrix, a is a 5-row × 1-column matrix, and **I** is a 7-row × 1-column unitary matrix.

$$\begin{bmatrix} P_0(-\frac{3}{3}) & P_1(-\frac{3}{3}) & P_2(-\frac{3}{3}) & P_3(-\frac{3}{3}) & P_4(-\frac{3}{3}) \\ P_0(-\frac{2}{3}) & P_1(-\frac{2}{3}) & P_2(-\frac{2}{3}) & P_3(-\frac{2}{3}) & P_4(-\frac{2}{3}) \\ P_0\left(-\frac{1}{3}\right) & P_1\left(-\frac{1}{3}\right) & P_2\left(-\frac{1}{3}\right) & P_3\left(-\frac{1}{3}\right) & P_4\left(-\frac{1}{3}\right) \\ P_0(\ \frac{0}{3}) & P_1(\ \frac{0}{3}) & P_2(\ \frac{0}{3}) & P_3(\ \frac{0}{3}) & P_4(\ \frac{0}{3}) \\ P_0\left(+\frac{1}{3}\right) & P_1\left(+\frac{1}{3}\right) & P_2\left(+\frac{1}{3}\right) & P_3\left(+\frac{1}{3}\right) & P_4\left(+\frac{1}{3}\right) \\ P_0(+\frac{2}{3}) & P_1(+\frac{2}{3}) & P_2(+\frac{2}{3}) & P_3(+\frac{2}{3}) & P_4(+\frac{2}{3}) \\ P_0(+\frac{3}{3}) & P_1(+\frac{3}{3}) & P_2(+\frac{3}{3}) & P_3(+\frac{3}{3}) & P_4(+\frac{3}{3}) \end{bmatrix} \begin{bmatrix} a_0 \\ a_1 \\ a_2 \\ a_3 \\ a_4 \end{bmatrix} = \begin{bmatrix} 1 \\ 1 \\ 1 \\ 1 \\ 1 \\ 1 \\ 1 \end{bmatrix}. \quad (6)$$

Equation (6) is solved using weighted least squares; the normal equations can be expressed as follows:

$$P^T W P a = P^T W I, \quad (7)$$

where P^T is the transpose matrix of P and W is the weighted matrix. The elements of the square matrix $P^T W P$ (5 × 5) can be expressed as Equation (8), written as follows:

$$\sum_{i=-3}^{i=3} P_l(\frac{i}{3}) P_k(\frac{i}{3}) W_i. \quad (8)$$

where row l = 0, 1, 2, 3, 4 and column k = 0, 1, 2, 3, 4. The elements of $P^T W$ (5 × 1 vector) can be written as follows:

$$\sum_{i=-3}^{i=3} P_l(\frac{i}{3}) W_i, \quad (9)$$

In an LSFLP, each element $a_{l,i}$ (coefficients of Legendre polynomials) is determinate for each sample. For example, to calculate the value of $a_{l,-3}$ (in sample i = −3), the equations to be solved can be expressed using Equations (7) and (9):

$$P^T W P \begin{bmatrix} a_{o,-3} \\ a_{1,-3} \\ a_{2,-3} \\ a_{3,-3} \\ a_{4,-3} \end{bmatrix} = \begin{bmatrix} W_{-3} P_0(-1) \\ W_{-3} P_1(-1) \\ W_{-3} P_2(-1) \\ W_{-3} P_3(-1) \\ W_{-3} P_4(-1) \end{bmatrix}. \quad (10)$$

To calculate the other values of $a_{l,i}$, only the value of i in Equation (10) is changed. From Equation (10), vector $a_{l,i}$ is a matrix (A) with 5 rows and 7 columns, which can be expressed as shown in Equation (11).

$$A(5,7) = \begin{bmatrix} a_{0,-3} & a_{0,-2} & \cdots & a_{0,0} & \cdots & a_{0,+2} & a_{0,+3} \\ a_{1,-3} & a_{1,-2} & \cdots & a_{1,0} & \cdots & a_{1,+2} & a_{1,+3} \\ a_{2,-3} & a_{2,-2} & \cdots & a_{2,0} & \cdots & a_{2,+2} & a_{2,+3} \\ a_{3,-3} & a_{3,-2} & \cdots & a_{3,0} & \cdots & a_{3,+2} & a_{3,+3} \\ a_{4,-3} & a_{4,-2} & \cdots & a_{4,0} & \cdots & a_{4,+2} & a_{4,+3} \end{bmatrix}. \quad (11)$$

If Equation (11) is known, then we can interpolate the first three and last three data points of the function being filtered by applying Equation (3). We can also say that the coefficient value represents a weighted value for the contribution of each sample.

Figure 2 shows a flux diagram describing the filtering process. Through trial and error, it was found that the first iteration still presented values with RN. In the second iteration, the RN decreased, but with a third, the relative error became very low and convergent.

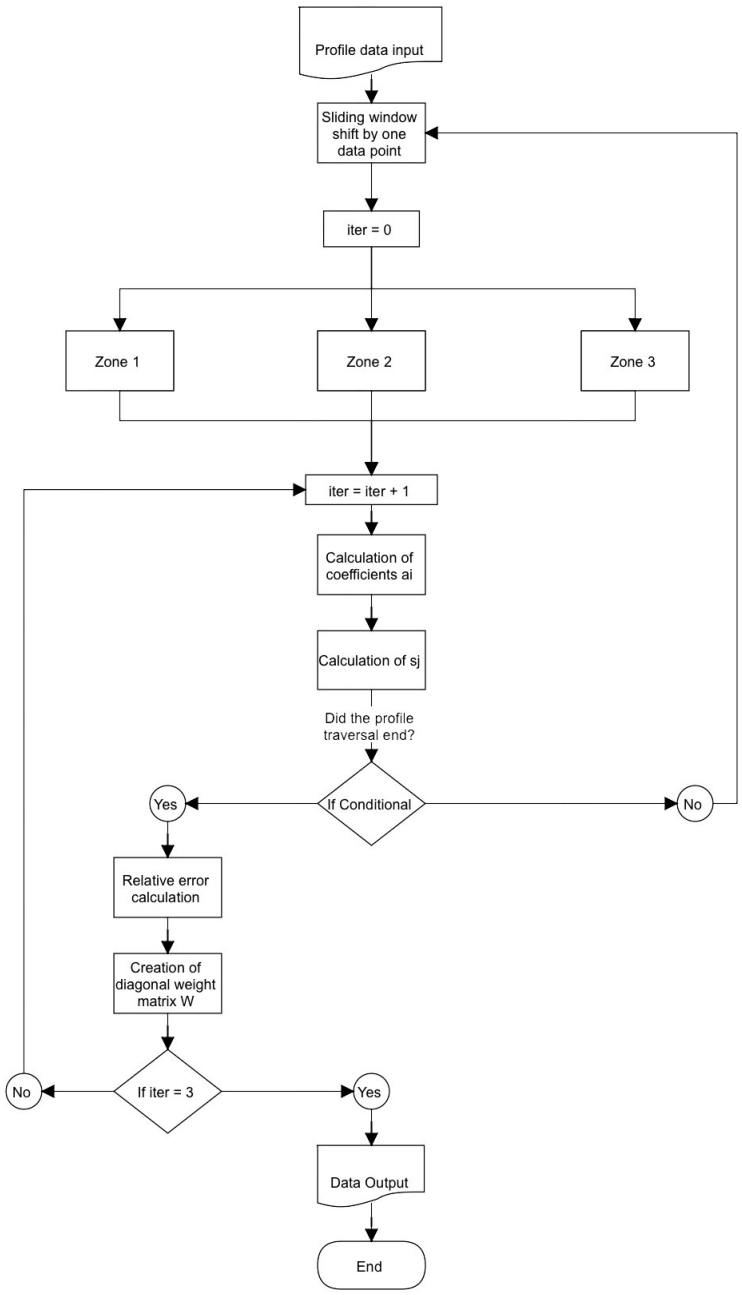


Figure 2. Flow chart of the proposed filtering method with three iterations.

2.3. Error and Weighted W Functions

In a traditional LSF, the coefficients remain constant; however, the LSFLP was designed as a least-mean-squares adaptive filter algorithm, which can be summarized as a two-step procedure to smooth ERT data [35]:

- Filtering process: An input signal produces a computing output response from a linear filter, and an estimation error is generated by comparing this output to a desired or reference signal.
- Adaptive process: This process involves the automatic adjustment of the parameters of the filter in accordance with the error estimation.

The coefficients are updated in each iteration to decrease the error of a reference signal (r_j), which is considered a freed signal of noise and the output signal (s_j) (Figure 3).

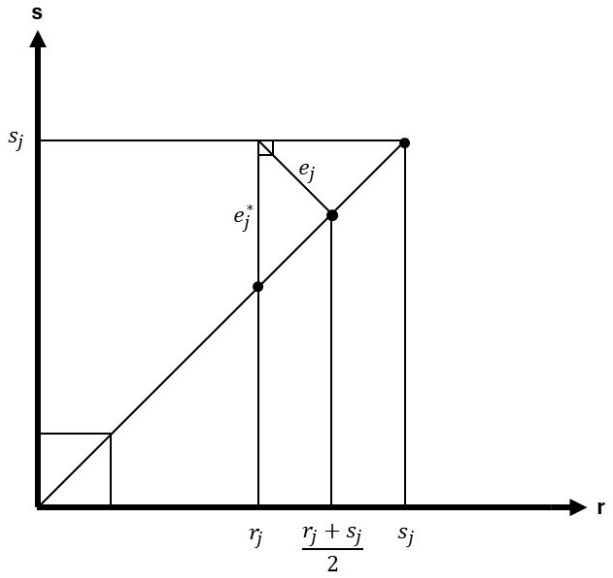


Figure 3. r_j is the profile data or a function to be filtered; s_j is the filtered function; $e_j^* = (r_j - s_j)$; $e_j = \frac{e_j^*}{\sqrt{2}}$; and the relative error is $Re_j = \sqrt{2}\left(\frac{r_j - s_j}{r_j + s_j}\right)$.

$$e_j^* = r_j - s_j. \tag{12}$$

The function error of Equation (12) is not adequate for electrical prospecting because the reference signal is free of noise or it is a known signal. Our reference signal is the same as the input signal; thus, it is also contaminated with noise. The question now is how to update the coefficients; the answer is that it can be solved by treating the LSFLP as a weighted least-squares filter. Thus, a better definition for the function error when both functions are contaminated with noise can be defined [22], written as follows:

$$e_j = \frac{e_j^*}{\sqrt{2}} = \frac{r_j - s_j}{\sqrt{2}}, \tag{13}$$

where the error is presented as the distance from the intersection point of e_j^* and s_j, which is projected onto a line at a forty-five-degree angle (Figure 2). If this projected point is lower than the horizontal axis, it would be $\frac{r_j + s_j}{2}$ (Figure 2). Based on Equations (12) and (13), a relative error function Re_j can be estimated to better deal with the error (Equation (14)).

$$Re_j = \sqrt{2}\left(\frac{r_j - s_j}{r_j + s_j}\right). \tag{14}$$

The elements of the weighted function W are defined as the inverse of the relative error function, written as follows:

$$W_j = abs\left(\frac{1}{Re_j}\right) = \frac{1}{\sqrt{2}} abs\left(\frac{r_j - s_j}{r_j + s_j}\right). \tag{15}$$

2.4. Proposed Smoothing Process and Correction Factor

The proposed smoothing process consists of correcting the stationary and transient voltages using a correction factor that eliminates or reduces the effects of unequal electrode spacing and unequal injected currents, such that the voltages collected in the field are only contaminated by systematic and random noise. Once the voltages are corrected, they are

filtered, and the new resistance, apparent resistivity, and chargeability are calculated. The new recalculated parameters are considered corrected and filtered.

The electrical anomaly for a homogeneous and isotropic half-space, where the electrode spacing and the injected current remain constant, is used to determine the correction factor.

2.4.1. Stationary Voltage Smoothing and Apparent Resistivity

The LSFLP has two valuable characteristics: (1) it preserves the shape of the function and (2) it maintains its peak values. However, one condition should be satisfied: the data should be equally spaced to obtain better filter performance. This condition is difficult to satisfy for field data. Therefore, it is worthwhile to study the apparent resistivity (ρ_a) as an anomaly since the resistivity value is expected to be constant for a homogeneous and isotropic half-space. If the values of ρ_a diverge from a constant value, it means that the half-space is heterogeneous, and different structures could be immersed in it. In Table 1, the electrical response of a homogeneous half-space is shown, where the spacing S among electrodes remains constant, and a fixed current of 1000 mA was applied. In Table 1, the apparent resistivity, voltage, and voltage/current (resistance) values show a linear behavior. However, in Table 2, where the current and spacing S were not constant, the voltage and voltage/current no longer showed linear behaviors (Figure 4).

Table 1. Values from a constant depth in a homogeneous half-space.

x (m)	FGFs	Current (A)	Voltage (V)	(V/A)	ρ_a
7.54	31.57	1000	3167.56	3.17	100
12.56	31.57	1000	3167.56	3.17	100
17.58	31.57	1000	3167.56	3.17	100
22.61	31.57	1000	3167.56	3.17	100
27.63	31.57	1000	3167.56	3.17	100
32.66	31.57	1000	3167.56	3.17	100
37.68	31.57	1000	3167.56	3.17	100
42.70	31.57	1000	3167.56	3.17	100
47.73	31.57	1000	3167.56	3.17	100
52.75	31.57	1000	3167.56	3.17	100

Linear behaviors for voltage (V), resistance (V/A), and apparent resistivity (ρ_a) were obtained from a horizontal line (x (m)) at a depth of 2.6 m in a homogeneous and isotropic half-space medium. The data were collected with a constant current (A) and equal spacing between electrodes. FGFs: field geometric factors.

Table 2. Comparison of field and corrected data with unequal electrode spacing.

Geometric Factor		Field Data				Corrected Data		
Field	Theoretical	(A)	(V)	(V/A)	ρ_a	V	(V/A)	ρ_a
1	2	3	4	5	6	7	8	9
29.49	31.57	1000	3390.979	3.390979	107.0532	3167.56414	3.167564	100
39.46	31.57	1000	2534.211	2.534211	80.00506	3167.56414	3.167564	100
27.03	31.57	900	3329.633	3.699593	116.7961	3167.56414	3.167564	100
37.36	31.57	900	2408.993	2.676659	84.50214	3167.56414	3.167564	100
28.95	31.57	900	3108.808	3.454231	109.0500	3167.56414	3.167564	100
32.82	31.57	810	2468.007	3.046922	96.19134	3167.56414	3.167564	100
26.13	31.57	891	3409.873	3.827018	120.8189	3167.56414	3.167564	100
37.47	31.57	801.9	2140.112	2.668801	84.25406	3167.56414	3.167564	100
23.29	31.57	882.09	3787.419	4.293688	135.5517	3167.56414	3.167564	100
41.43	31.57	793.881	1916.198	2.413709	76.20082	3167.56414	3.167564	100

Columns 4, 5, and 6 depict the behaviors when the condition of Table 1 is not satisfied. Columns 7, 8, and 9 depict the behaviors when a corrected factor CF (Equation (14)) is applied.

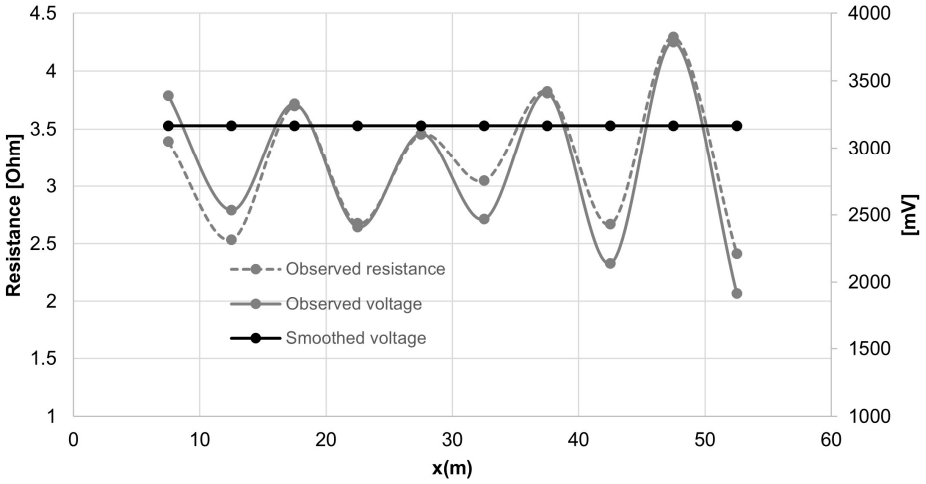


Figure 4. Observed voltage and resistance when current and electrode spacing are not constant. A smoothed voltage is recovered after correction.

However, it is important to emphasize that the voltage measured in the field is correct, and if the apparent resistivity is calculated with the real field geometric factor (FGF) for a half-space or topographic relief, it would also be correct. However, most of the time, it is not possible to precisely position the electrodes. Therefore, it is suggested to measure the actual distances to calculate the real geometric factor (FGF).

$$FGF = 2\pi\left(\frac{1}{AMF} - \frac{1}{BMF} - \frac{1}{ANF} + \frac{1}{BNF}\right)^{-1}, \tag{16a}$$

where AMF, BMF, ANF, and BNF are the distances between electrodes, obtained as a function of the field coordinate positions.

On the other hand, when calculating the apparent resistivity, it is customary to use a theoretical geometric factor (*TGF*), which is calculated by considering a constant spacing between electrodes (16b) that leads to the wrong apparent resistivity value (Table 2, column 6) and the creation of spurious anomalies [33,36–38].

$$TGF = 2\pi\left(\frac{1}{AMT} - \frac{1}{BMT} - \frac{1}{ANT} + \frac{1}{BNT}\right)^{-1}, \tag{16b}$$

where AMT, BMT, ANT, and BNT are the distances between electrodes, obtained as a function of the theoretical coordinate positions.

A correction factor should be applied to the collected voltages, such that all three parameters have a linear behavior (i.e., as if the medium was a homogeneous and isotropic half-space). This can be achieved under two conditions: (1) equal spacing between electrodes and (2) with the application of an arbitrary constant current of 1000 mA (Table 1).

To determine the correction factor (*CF*), we assume that the subsoil is a homogeneous and isotropic half-space. It is important to establish that the corrected data will reflect the surface of the true terrain (topography), whether rough or flat, and only the spacing between electrodes is corrected to an equal spacing, and the injected current is kept constant. The steady and transient voltages, as well as the apparent resistivity and chargeability, are all functions of the spatial coordinates (x, y, and z), and the transient voltage is a function of time. Spatial coordinates, except for the temporal variable, are not written explicitly to make the writing more concise.

The observed ρ_a will remain unaltered after correction. Thus, from the definition of apparent resistivity, the following is obtained:

$$\frac{V_c}{I_c} TGF = \frac{V_f}{I_f} FGF. \tag{16c}$$

The sub-indexes c and f define the corrected and observed parameters for voltage V and current I, respectively. I_f is the real current injected into the subsoil, TGF is the theoretical geometric factor, and FGF is the field geometric factor.

From Equations (16a)–(16c), the corrected voltage (V_c) is as follows:

$$V_c = V_f \left(\frac{I_c}{I_f} \frac{FGF}{TGF} \right). \tag{17}$$

From Equation (17), the correction factor (CF) is defined as follows:

$$CF = \frac{I_c}{I_f} \frac{FGF}{TGF}. \tag{18}$$

The corrected resistance R_c is defined as follows:

$$R_c = \frac{V_c}{I_c} = \frac{V_f}{I_c} CF = \frac{V_f}{I_f} \left(\frac{FGF}{TGF} \right). \tag{19}$$

The corrected apparent resistivity $\rho_{a,c}$ will be unaltered and is expressed as follows:

$$\rho_{a,c} = R_c TGF = \frac{V_f}{I_f} \left(\frac{FGF}{TGF} \right) TGF. \tag{20}$$

By applying Equations (17)–(20) to the field data in Table 2, we obtain the corrected data (columns 7–9). However, if the half-space is a heterogeneous medium, the corrected voltage, corrected resistance, and corrected apparent resistivity will show the same deviation from linear behavior.

Once the voltage is corrected, it is smoothed by applying the proposed LSFLP (Equations (2) and (3)) to obtain the corrected and filtered $V_{c,f}$ voltage, $R_{c,f}$ resistance, and $\rho_{a,f}$ apparent resistivity.

2.4.2. Transient Voltage Smoothing and Chargeability

It is important to note that chargeability data are not collected in the field. Chargeability (μ) is the relationship between the transient voltage $V_f(t)$ and the stationary voltage V_f, both of which are acquired in the field but at different moments. We used the instantaneous chargeability, as defined by [20], to clarify the filtering procedure for this parameter, written as follows:

$$\mu(t) = \frac{V_f(t)}{V_f}. \tag{21}$$

According to Equation (14) where V_f has been corrected to be filtered, $V_f(t)$ should be corrected and a corrected chargeability μ_c should be defined. $V_f(t)$ is measured in the field but is not recorded; it can be recovered using Equation (21), written as follows:

$$V_f \mu(t) = V_f(t). \tag{22}$$

Equation (22) is applicable if you have equipment capable of recording the IP drop curve in at least 20 time windows. In a case where only the overall chargeability is recorded, Equation (22) can still be applied.

The transient voltage must be corrected before any filtering process is applied. In Equation (22), V_f (stationary voltage) is substituted with its corrected value (Equations (17) and (18)) to obtain the following:

$$V_c(t) = V_f(t)CF = V_f CF\mu_f(t). \tag{23}$$

Based on the previous equations, it is possible to define the following:

$$\mu_c(t) = \frac{V_f CF\mu_f(t)}{V_f CF} = \mu_f(t). \tag{24}$$

The corrected chargeability (Equation (24)) is not the filtered function. The corrected transient voltage $V_c(t)$, defined by Equation (23), is the one that is filtered; we then obtain a filtered $V_{c,f}(t)$. $V_{c,f}(t)$ is a function of time and distance, so it should be filtered in terms of both variables (the same LSFLP filter is applied). The new corrected and filtered chargeability can be recovered using Equation (25), written as follows:

$$\mu_{c,f}(t) = \frac{V_{c,f}(t)}{V_{c,f}}. \tag{25}$$

However, there is a question of whether Equation (25) provides a valuable smoothed $\mu_{c,f}(t)$ chargeability function of $\mu_f(t)$. To answer this, it is important to analyze the chargeability from the point of view of the expected value if there is a relationship between two functions contaminated with RN. Since they were recorded at different times, they are considered uncorrelated.

The following is well known:

$$\mathbb{E}\Big(V_f\Big) = \mathbb{E}\Big(V_f + \delta_f\Big) = \hat{V}_f, \tag{26a}$$

$$\mathbb{E}\Big(V_f(t)\Big) = \mathbb{E}(\hat{V}_f(t) + \delta_t) = \hat{V}_f(t), \tag{26b}$$

where $\mathbb{E}$ is the expected value, and δ_f and δ_t are the RN functions for the stationary and transient voltages, respectively.

The expected value for chargeability can be calculated as follows:

$$\mathbb{E}(\mu(t)) = \mathbb{E}\left(\frac{\hat{V}_f(t) + \delta_t}{\hat{V}_f + \delta_f}\right) = \mathbb{E}\left(\frac{\hat{V}_f(t)}{\hat{V}_f}\left(1 + \frac{\delta_t}{\hat{V}_f(t)}\right)\left(1 + \frac{\delta_f}{V_f}\right)^{-1}\right). \tag{27}$$

Using the Newton general binomial and calculating the product, we obtain the following:

$$\mathbb{E}(\mu(t)) = \mathbb{E}\left(\frac{\hat{V}_f(t)}{\hat{V}_f} + \frac{\hat{V}_f(t)}{\hat{V}_f}\frac{\delta_t}{\hat{V}_f(t)} - \frac{\hat{V}_f(t)}{\hat{V}_f}\frac{\delta_f}{V_f} - \frac{\hat{V}_f(t)}{\hat{V}_f}\frac{\delta_t\delta_f}{\hat{V}_f(t)V_f} + \cdots\right). \tag{28}$$

The expected value for chargeability from Equations (26) and (28) can be expressed as follows:

$$\mathbb{E}(\mu(t)) = \mathbb{E}\left(\frac{\hat{V}_f(t)}{\hat{V}_f}\right) = \frac{\hat{V}_f(t)}{\hat{V}_f} = \frac{\mathbb{E}\Big(\hat{V}_f(t) + \delta_t\Big)}{\mathbb{E}\Big(\hat{V}_f + \delta_f\Big)}. \tag{29}$$

If we now consider the ratio of the expected values of V_f and $V_f\,(t)$, then from Equation (29), we obtain the following:

$$\frac{\mathbb{E}\left(V_f(t)\right)}{\mathbb{E}\left(V_f\right)} = \frac{\mathbb{E}\left(\hat{V}_f(t) + \delta_t\right)}{\mathbb{E}\left(\hat{V}_f + \delta_f\right)} = \frac{\hat{V}_f(t)}{\hat{V}_f} = \mathbb{E}(\mu(t)). \tag{30}$$

Equation (30) is a second-order approximation, which means the following:

$$\left| \mathbb{E}\left(\frac{V_f(t)}{V_f}\right) - \frac{\mathbb{E}\left(V_f(t)\right)}{\mathbb{E}\left(V_f\right)} \right| \sim \mathcal{O}(2). \tag{31}$$

Then, from Equation (30), it is possible to deduce that the expected value of the ratio $\frac{\hat{V}_f(t)}{\hat{V}_f}$ would be equal to the ratio of the expected values of $V_f\,(t)$ and V_f.

Based on Equations (25) and (30), it is possible to state the following:

$$\mathbb{E}\left(\frac{V_f(t)}{V_f}\right) = \mathbb{E}\left(\frac{V_{c,f}(t)}{V_{c,f}}\right) = \mu_{c,f}(t), \tag{32}$$

where $\mu_{c,f}(t)$ is the chargeability, $V_{c,f}\,(t)$ is the transient voltage, and $V_{c,f}$ the stationary voltage, where all three functions have been corrected and smoothed. Figure 2 shows the flow chart of how both the correction factor (CF) and the filter (LSFLP) are applied. Figure 5 depicts a flow chart of the correction and filtering process that is applied to electrical data.

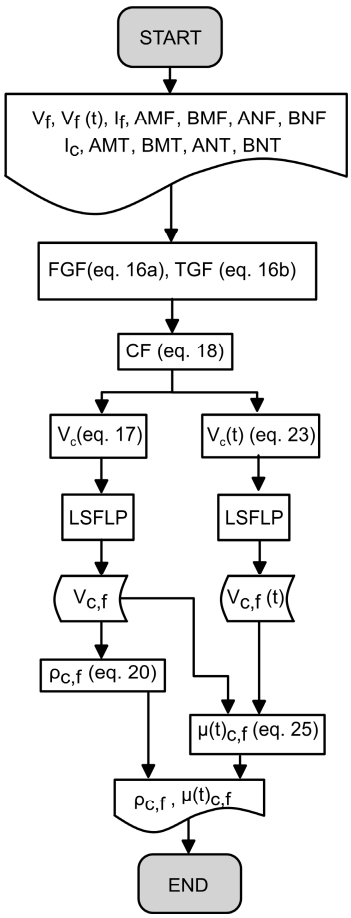


Figure 5. Flow chart of the proposed method for filtering and correcting the resistivity and IP response.

3. Results

3.1. Archaeological Site of Mitla

The ruins of Mitla are the remains of an ancient Zapotec city originally called Lyobaa, the sacred city for the veneration of death, and whose apogee occurred during the postclassic period, between 1200 and 1521 AD, when it concentrated the political and religious power of the central valleys of Oaxaca, Mexico. The architectural group known as the Calvary Group belongs to Mitla's archaeological zone. It has a quadrangular plaza surrounded by four mounds dating back to the early stages of the Zapotec occupation of Mitla. The largest of these mounds, located to the east of the complex, is in the shape of a 9 m tall, stepped pyramid built of adobe, with its main stairs facing west. In 1547, a chapel, known by the locals as El Calvario (the Calvary), was built in the upper part of this pyramid (Figure 6). It is worth noting that the existence of this historic chapel has prevented archaeological explorations of this mound. Figure 3 shows El Calvario chapel and its 2D Schlumberger–Wenner profile.



Figure 6. El Calvario (the Calvary) and its 2D Schlumberger–Wenner profile.

An ERT2D analysis with a Schlumberger–Wenner array was carried out on El Calvario to study the conditions of the ground under the pyramid (Figure 7). The Schlumberger–Wenner profile was designed with an electrode spacing of 1.5 m, and 34 electrodes were used. Because the topography is rough, the data were corrected to a flat topography, as suggested in [32], to improve the performance of the inversion program employed for analyzing the ERT2D data.

The El Calvario field data were first inverted without using the process proposed in this article. Afterwards, the field data were filtered (no correction was applied) and inverted, and finally, the field data were corrected, filtered, and inverted. Three smoothing filters were applied: a moving average (MA) filter, a Savitzky–Golay (SG) filter (using an inner subroutine available from Python software 3.7), and finally the proposed LSFLP.

Table 3 shows the parameters and the commercial inversion software used. It is worth mentioning that the three filters allowed a damping factor of 10 and a smoothing factor of 1 with only a minor amount of data requiring manual removal. An outer loop of 2 iterations and an inner loop of 12 iterations were used for all the inversions.

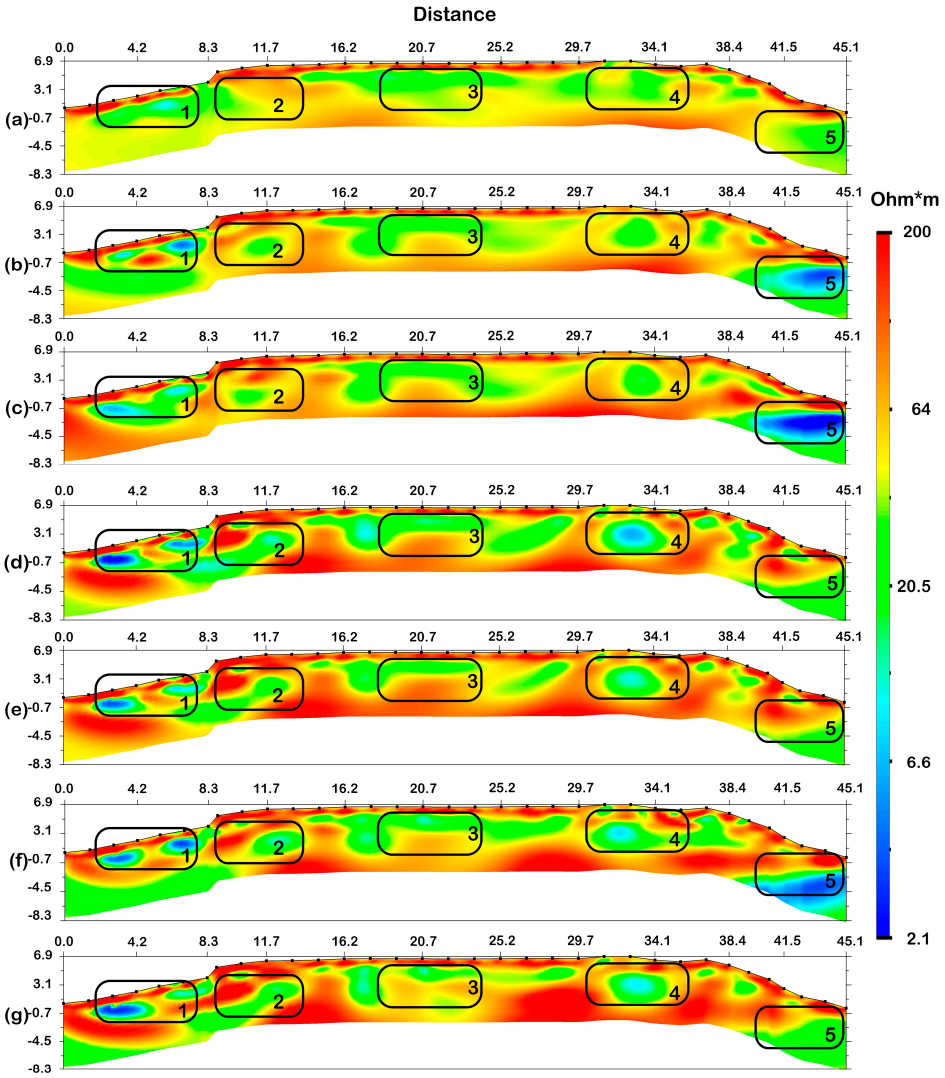


Figure 7. ERT2D images of the Calvary. Seven resistivity sections were obtained from the following data: (**a**) raw resistivity data; (**b**) MA-filtered data; (**c**) MA-filtered and corrected data; (**d**) SG-filtered data; (**e**) SG-filtered and corrected data; (**f**) LSFLP-filtered data; and (**g**) LSFLP-filtered and corrected data.

Table 3. Inversion data from each section in Figure 7.

	Initial Data	Final Data	Discarded Data	RMS%	L2-Norm	Damping Factor	Smoothing Factor
Raw Data	247	227	20	0.40	0.02	10.0	1.0
MA-Filtered	247	227	20	0.97	0.10	10.0	1.0
MA-Filtered and Corrected	247	236	11	0.98	0.11	10.0	1.0
SG-Filtered	247	235	12	2.05	0.47	10.0	1.0
SG-Filtered and Corrected	247	235	12	2.05	0.47	10.0	1.0
LSFLP-Filtered	247	238	9	2.05	0.47	10.0	1.0
LSFLP-Filtered and Corrected	247	236	11	2.43	0.66	10.0	1.0

Moving average (MA), Savitzky–Golay (SG), and least-squares weighted filter with Legendre polynomial as basis function (LSFLP).

From Table 3, it can be observed that 20 data points were manually discarded from the field data (without applying filtering or corrections). The RMS and L2-Norm errors in the inversion process were the lowest (0.40% and 0.02%). Using the moving average filter, 20 data points were manually discarded after only filtering and inversion, and when they

were filtered, corrected, and inverted, only 11 data points were discarded. The errors of the moving average inversions remained low and acceptable.

However, when the Savitzky–Golay filter was applied to the El Calvario data, 12 data points were manually discarded (from filtered data and filtered and corrected data), but the errors remained low and equal for both cases (RMS: 2.05%; L2-Norm: 0.47%). Using the LSFLP filter data (only filtered and inverted), nine data points were discarded, and the errors were 2.05% and 0.47%. When the data were filtered and corrected, 11 data points were discarded, and the errors slightly increased to 2.43% and 0.66%.

The greatest discrepancies between the different inverted profiles were found towards the sides of the structure. On the left side of the structure (Figure 7, box 1), the greatest discrepancy in the raw data profile (Figure 7a), which does not define the different sections (resistivity around 40 Ohm*m, yellow color), was the presence of two low-resistivity rounded anomalies enclosed by a high-resistivity medium, where resistivity values similar to those of the right side were expected (box 5, resistivity around 20 Ohm*m, green color) due to similar filling materials and slopes. In boxes 1 and 2 (Figure 7), there were better correlations between the MA, SG, and LSFLP filters, although the correlations were weaker for MA.

The analysis of the profiles of the right flank of the structure (boxes 4 and 5) showed better correlations between the filters used, especially box 4.

The analysis of the central part of El Calvario (box 3) is important because of the high probability that there is a hall at the top of the buried pyramid (centered at X = 22.5 and Z = 3.0 m), but so far, no excavation has been carried out at that site due to the existence of the historic chapel of the Calvary.

The analysis of the central part of the ERT profile using the different filters clearly showed the existence of a possible hall (on the top, horizontal side, and two vertical limits). However, the raw data profile did not show the existence of such a structure. The LSFLP profile showed better definition of a hall (a high-resistivity rectangular shape, surrounded by a medium-to-low-resistivity medium), but so far, no excavation has been carried out at this site.

In summary, the left flank produced the noisiest data; however, the LSFLP-inverted image showed better agreement with the filtered-only data (Figure 7f) and the filtered and corrected image (Figure 7g; fewer transitions between red and green and between green and dark blue) (see Table 4). On the right flank, the filtered and the filtered and corrected images (Figure 7b–g) showed a good agreement, especially in box 4.

Table 4. Qualitative interpretation of Figure 4.

Section	Name	Best Definition of Left Side Flank (Box 1)	Best Definition of Possible Hall, Vertical and Horizontal Sides (Box 3)	Coherent Flank Sides (Boxes 2 and 4)	Coherent Bottom Side (Box 5, Green Color)
(a)	Raw Data				
(b)	MA-Filtered				
(c)	MA-Filtered and Corrected	X			
(d)	SG-Filtered			X	X
(e)	SG-Filtered and Corrected	X		X	X
(f)	LSFLP-Filtered			X	
(g)	LSFLP-Filtered and Corrected	X	X	X	X

X indicates that the section showed the attribute in the column heading.

Finally, in the central area (box 3), the filtered and the filtered and corrected images (Figure 7b–g) showed the existence of a structure (a possible hall), which is better defined

than in Figure 7g. The raw data (Figure 7a) do not indicate the existence of the structure, and a possible explanation could be that the data were not corrected for a flat surface.

Tables 3 and 4 show, with the SG and LSFLP filters, the best definition of the flank sides and less discarded data. However, the LSFLP-filtered data had less discarded data and similar RMS and L2-Norm errors compared to the SG filter (filtered and filtered and corrected data).

To visualize where the hall response can be detected in Figure 8, the resistance curve for a depth of 3 m is depicted. The electrical resistivity response of the hall can be visualized at X = 22.5 m.

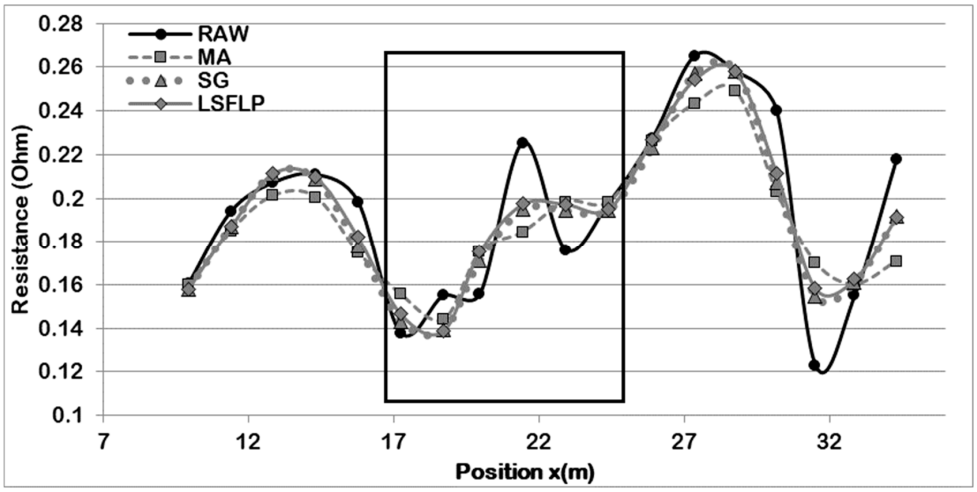


Figure 8. The hall response is centered at X = 22.5 m (rectangular box). Raw (original data), and moving average (MA)-, Savitzky–Golay (SG)-, and a least square weighted filter with Legendre polynomial (LSFLP)-filtered data.

3.2. Hydrocarbon-Contaminated Site North of Mexico City

This study area is within the Mexican Neovolcanic Belt and is located towards the northern part of Mexico City, a heavily populated metropolis. This place used to be an important refinery owned by a Mexican oil company. Today, this plant has been converted into a park and a place of coexistence for the surrounding population. On the other hand, this place has also become a huge laboratory that has allowed soil researchers to learn about the effects of hydrocarbons in the subsoil. Exploration methods, such as ERT-2D, have been of great help in detecting electrical anomalies that correspond to regions with high pollutant concentrations.

The zone is made up of volcanic–sedimentary materials from the Guerrero Terrain, covered by alluvium of sedimentary rocks from the Zimapán basin [39]. Superficially, the site is covered by a gently sloping fill. There was no evidence of a regular distribution of sand and silts and there is information about a body of water around 3.5 m deep. The geological and pedological studies of this place showed that the study area was in chaos, and lenses of sand, silt, and clay were found, many of which were produced by the rise and fall of the surrounding water bodies. These strong variations at different depths have caused further oil pollution.

Therefore, the aim of this study was to delimit the contaminated regions through the anomalies (resistivity and chargeability anomalies) produced by hydrocarbons (benzene). The hydrocarbon-contaminated site (HC) data were inverted without applying the proposed process. Then, these data were corrected, filtered, and inverted. Three smoothing filters were applied: MA, SG, and LSFLP. Figure 9 shows the results for seven dipole–dipole resistivity sections (left column) and their corresponding IP sections (right column).

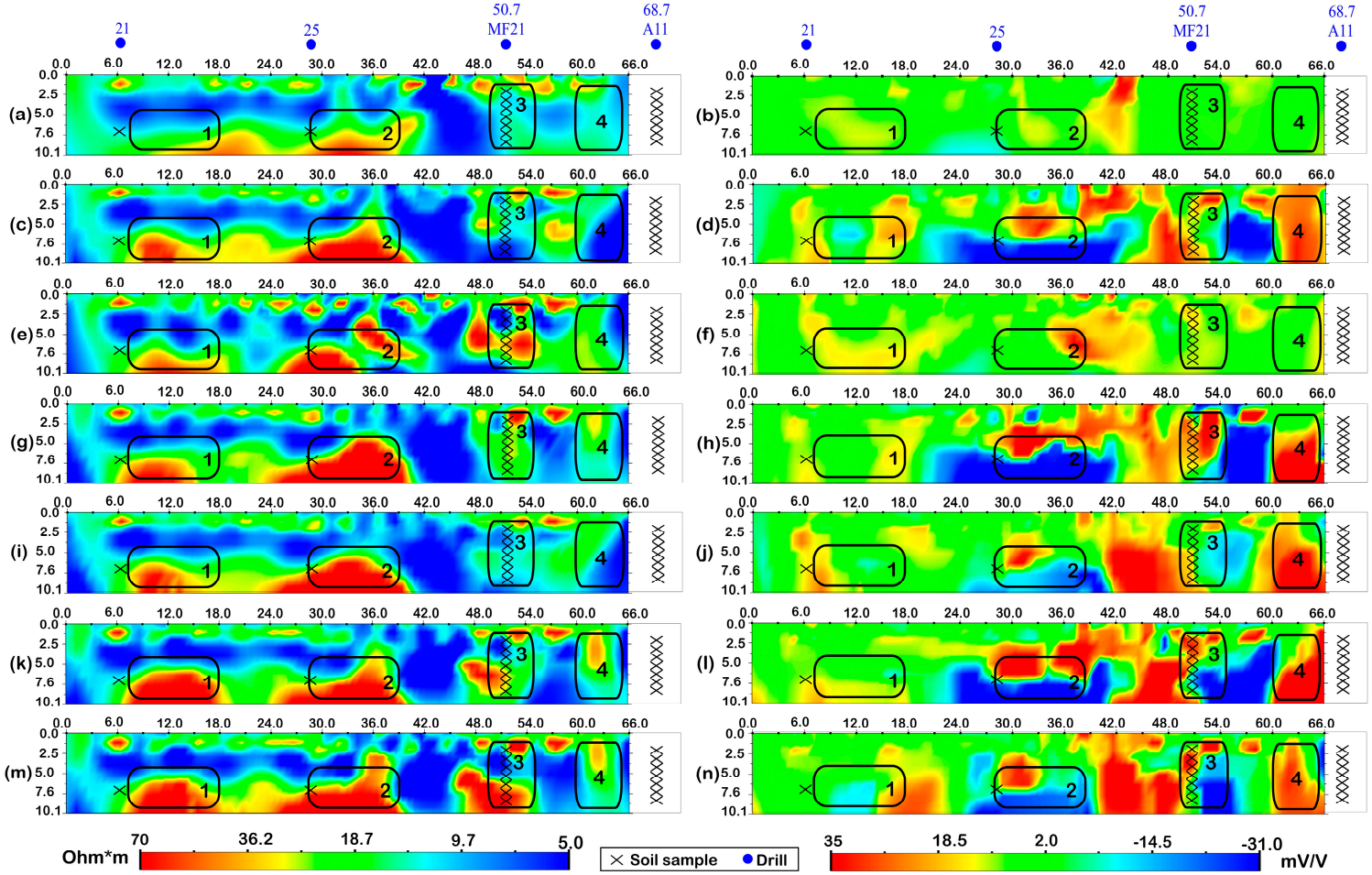


Figure 9. Hydrocarbon-contaminated sections. Seven resistivity sections were obtained: (**a**) raw resistivity section and (**b**) its IP section; (**c**) MA-filtered resistivity data section and (**d**) its IP section; (**e**) MA-filtered and corrected data and (**f**) its IP section; (**g**) SG-filtered data and (**h**) its IP section; (**i**) SG-filtered and corrected data and (**j**) its IP section; (**k**) LSFLP-filtered data and (**l**) its IP section; and (**m**) LSFLP-filtered and corrected data and (**n**) its IP section. Drill names 21, 25, MF21, and A11 are shown at the top of the figure in each column. Red represents high values; blue represents low values.

The resistivity sections (left side in Figure 9) showed low values (5 Ohm*m, shown as blue) around a depth of 3 m and in boxes 1–3. These anomalies correlated with the body of water described above. In addition, all the resistivity sections exhibited anomalies with similar patterns, except for the IP anomalies (right side in Figure 9): Figure 9b,f (box 2) does not exhibit the low IP responses (dark blue color) seen in the rest of the sections (Figure 9d,h–n). Another situation occurred in the zone within box 4: Figure 9b,f show green IP responses (around 2 mV/V), while the others showed high IP values (35 mV/V in Figure 9d,h–n). It is also interesting that there were anomalies between boxes 2 and 3 (Figure 9d,f,h,j,l,n), where the high (red) IP values showed different patterns. However, these anomalies were similar between Figure 9h (SG-filtered) and Figure 9l (LSFLP-filtered) and between Figure 9j (SG-filtered and corrected) and Figure 9n (LSFLP-filtered and corrected).

It is important to note that a negative IP response is related to the internal chargeability values that the bodies present. If a smaller IP-response body is embedded in a larger IP-response body, the anomaly would be negative. Very low IP responses may respond to moisture content.

Additional information is presented in Tables 5 and 6. Table 5 shows the data of benzene concentrations in soil and water obtained in some points collected at different locations in the study area. At the time of data acquisition, there was a PVC pipe installed in a well (MF21) located at position x = 50.7 m (Figure 9). Furthermore, it is important to mention that the half-left zone was almost remediated before the geoelectrical data were recorded.

Table 5. Benzene concentration in the soil and water samples.

Depth (m)	21 (mg/L)	25 (mg/L)	MF21 (mg/kg)	A11 (mg/kg)
1.2			0.78	0.80
2.4			3.46	0.82
3.6			57.77	19.17
4.8			362.79	21.90
6.0			860.55	157.06
7.2 *	40.891	399.753	265.85	507.23
8.4			3329.74	896.92

* Only two water samples were collected: one at drill number 21 and one at drill number 25.

Table 6. Inversion data from each section in Figure 9.

		Initial Data	Final Data	Discarded Data *	RMS %	L2-Norm
Raw data	Resistivity Chargeability	189	171	18	16.27 37.87	0.25
MA-filtered	Resistivity Chargeability	189	176	13	6.99 18.92	0.52
MA-filtered and corrected	Resistivity Chargeability	189	168	21	4.78 6.83	2.53
SG-filtered	Resistivity Chargeability	189	166	23	7.59 15.21	0.60
SG-filtered and corrected	Resistivity Chargeability	189	171	17	4.74 10.74	0.53
LSFLP-filtered	Resistivity Chargeability	189	164	25	10.85 14.75	0.57
LSFLP-filtered and corrected	Resistivity Chargeability	189	174	15	10.84 11.32	0.72

* Data were discarded using a tool within the inversion software, which suggests which data to delete to obtain a better RMS value. This option is displayed using a histogram data option.

Table 6 shows that each section had the same number of initial data points (189). The smoothing and inversion damping factors were set to 10 for all sections. The number of discarded data points ranged from a minimum of 13 (MA-filtered) to a maximum of 25 (LSFLP-filtered). The RMS error values varied between 4.78 (MA-filtered and corrected) and 15.17 (SG-filtered) for resistivity and 6.83 (MA-filtered and corrected) to 37.87 (raw data inversion) for IP. The L2-Norm ranged from a minimum of 0.25 (for raw data inversion) to a maximum of 2.53 (for MA-filtered and corrected data). Additionally, five sections exhibited IP RMS values approximately two-fold higher than the resistivity RMS values (raw data inversions, MA-filtered, MA-filtered and corrected, SG-filtered, and SG-filtered and corrected). Two sections, however, showed low RMS values for both resistivity and IP within the same range; these sections had the fewest discarded data points (MA-filtered and corrected data: RMS values of 4.78 and 6.83, and 13 discarded data points; LSFLP-filtered and corrected data: RMS values of 10.84 and 10.29, and 15 discarded data points). Notably, the MA-filtered and corrected data had the highest L2-Norm (2.53), while the LSFLP-filtered and corrected section showed a significantly lower L2-Norm (0.72).

The left side of all the IP sections (boxes 1 and 2) had moderate IP values (green color; around 2 mV/V). This behavior can be explained by the remediation process mentioned earlier. However, within box 1, some IP sections (d, j, and n) had light blue anomalies (−12 mV/V) in front of the orange-yellow medium (31–12 mV/V), showing that there were contaminants remaining in this zone (see Table 7).

Table 7. Inversion data for each section in Figure 9.

	IP Section	Traces of Contamination (Box 1)	Existence of Low IP (Box 2)	PVC Pipe Definition (Box 3)	High IP Response Due to Contamination (Box 4)
(b)	Raw Data				
(d)	MA-Filtered	X	X		X
(f)	MA-Filtered and Corrected				
(h)	SG-Filtered		X		X
(j)	SG-Filtered and Corrected	X	X		X
(l)	LSFLP-Filtered		X		X
(n)	LSFLP-Filtered and Corrected	X	X	X	X

X indicates that the section showed the attribute in the column heading.

Box 2 also exhibited various anomalies. Figure 9b,f do not show a low IP response (dark blue; −31 mV/V), whereas Figure 9d,h,j,l,n do.

Analyzing box 3 using soil sample data from Table 5 revealed strong red anomalies (70 Ohm*m) correlated with high benzene concentrations (up to 860.55 mg/kg for MF21 and 507.23 mg/kg for A11). This was particularly evident in Figure 9k,l (LSFLP-filtered) and Figure 9m,n (LSFLP-filtered and corrected), where high values were observed for both resistivity and IP. A closer examination of Figure 6 shows a well-defined vertical anomaly structure in box 3 in the soil samples, which was approximately 1.5 m in diameter and extended almost the entire depth of the section. This structure corresponds to the PVC pipe mentioned above.

In box 4 in Figure 9b (raw IP data inversion) and 9f (MA-filtered and corrected data), the IP responses showed moderate values (around 2 mV/V). This geoelectrical response indicated that this zone was not contaminated. However, the other IP sections (Figure 9d,h,j,l,n) showed the opposite (high IP values: 35 mV/V; red color). Moreover,

the anomaly in box 4 had different shapes and lengths. Nevertheless, the SG-filtered data (Figure 9h) were similar to the LSFLP-filtered data (Figure 9l), and the SG-filtered and corrected data (Figure 9j) were similar to the LSFLP-filtered and corrected data (Figure 9n).

In summary, based on Figure 9 and Tables 5–7, sections (m) and (n) demonstrated that the LSFLP-filtering and correction approach is the best option, both mathematically and qualitatively. The samples from drill number MF21 (box 3) and A11 exhibited high benzene concentrations with increasing depth (Table 5). At MF21, there was a decrease in the benzene concentration at the bottom (265.85 mg/kg at a depth of 7.2 m). The resistivity (Figure 9m) and IP (Figure 9n) responses of the samples from these two drills correlated well. In addition, these two sections achieved good L2-Norm values, minimal data losses, and consistent RMS values for their resistivity and IP responses.

4. Discussion

4.1. El Calvario (The Calvary) Archaeological Zone in Mitla

The analysis of the errors obtained from the ERT2D images of the archaeological site of El Calvario (Table 3) showed that both the RMS and the L2-norm values were low. From the analysis of the RMS and L2-norm errors alone, any of the seven inverted images (Figure 7) would be acceptable; however, there were differences between them depending on the filter applied and whether the correction factor was applied.

We will focus the discussion on the central area since we can analyze the contribution of the proposed smoothing filter and correction factor here. It is important to note that the subsoil of El Calvario has not been subject to any archaeological exploration, so if only the raw data section had been analyzed (Figure 7a), the possible existence of the hall would have gone unnoticed. The ERT2D data (Figure 7b–g) filtered and corrected using the moving average (MA), Savitsky–Golay (SG), and least-squares Legendre filter (LSFPL) filters showed the existence of a rectangular structure (box 3). The use of the MA filter showed a well-defined and isolated hall (Figure 7b,c), while the SG-filtered data showed a slightly longer hall (Figure 7d,e).

Finally, the inverted ERT2D data filtered using the LSFLP showed evidence of the possible existence of a well-defined hall (Figure 7f–g), especially the image shown in Figure 7g. In summary, the ERT2D study of El Calvario shows the valuable contribution of applying a smoothed filtering and correction factor for ERT2D data collected in difficult terrain to improve inversion models.

4.2. Discussion of Hydrocarbon-Contaminated Site North of Mexico City

In the case of the hydrocarbon-contaminated site, differences were observed between the filtered and filtered and corrected datasets. For instance, in the resistivity data (left column of Figure 9) at the bottom of box 3, the MA-filtered and corrected (Figure 9e) and LSFLP-filtered and corrected data (Figure 9m) showed strong and defined anomalies with high resistivity values (red color). These anomalies correlated with high benzene concentrations. In contrast, these red anomalies did not appear in the filtered data (Figure 9c) and the SG-filtered sections (Figure 9g,i).

In box 3 in the IP sections (right side Figure 9), the SG-filtered and corrected section (Figure 9j) showed better correlation with benzene concentrations. However, the LSFLP-filtered and corrected section was unique in its delineation of a pipeline along the line where the soil samples were collected.

5. Conclusions

Any filtering process applied to a dataset influences the interpretation of the electrical anomalies. Therefore, it is recommended that the filter and any other process used to improve the data alter it as little as possible, particularly the original shape of the ERT and TDIPT anomalies. The proposed process of employing a smoothing filter and correction factor seeks to preserve these anomalies as much as possible. In the examples discussed, resistivity data from electrical resistive tomography was less affected by the smoothing filter used; however, the proposed LSFLP filter in the present paper showed a better performance, as deduced from the 2D electrical resistivity tomography results for the archaeological zone of Mitla in Southern Mexico.

To filter the resistivity data with the proposed process, it is recommended to use a maximum of three iterations and apply the correction factor (CF), in addition to collecting the field data level by level.

On the other hand, the chargeability anomaly was more affected by the treatment applied, as shown in the case of the soil contaminated with hydrocarbons. For the chargeability of the raw data, a clear correlation between resistivity anomalies and chargeability could not be defined, as expected.

Using the moving average filter produced a better result in terms of anomaly shape, and differences were observed between the filtered (Figure 9d) and filtered and corrected data (Figure 9f), but a better correlation between resistivity and chargeability could be established.

Using the Savitzky–Golay filter, a better image of the inverted chargeability was obtained, although there were some differences between the filtered (Figure 9h) and filtered and corrected data (Figure 9j).

Finally, in the ERT and TDIPT data, no correction was made for the electrode position; however, a constant current was applied.

It should be noted that the MA and Savitzky–Golay filters were used as feedback filters. It was not possible to apply a correction for electrode positioning, but a constant current of 1000 mA was applied.

Finally, the LSFLP-inverted chargeability images showed a better correlation with resistivity, but there were differences between the filtered (Figure 9l) and filtered and corrected data (Figure 9n). The LSFLP filter was designed as an iterative filter, and three iterations were allowed.

Author Contributions: Conceptualization, A.T.-A. and J.M.T.-A.; Methodology, A.T.-A., A.E.L.-G. and J.M.T.-A.; Software, A.T.-A.; Validation, A.T.-A.; Investigation, A.T.-A., A.E.L.-G. and J.M.T.-A.; Resources, A.E.L.-G.; Data curation, A.T.-A.; Writing—original draft, A.T.-A. and A.E.L.-G.; Writing—review & editing, A.T.-A., A.E.L.-G. and R.E.C.-S.; Visualization, A.E.L.-G.; Project administration, D.L.A.; Funding acquisition, D.L.A. All authors have read and agreed to the published version of the manuscript.

Funding: This research was funded by Asociación para la Investigación Arqueológica—ARX Project, A.C. and National Institute of Anthropology and History (INAH).

Data Availability Statement: The datasets presented in this article are not readily available because it is affiliation's property.

Acknowledgments: We would like to thank the geophysics team of the UNAM Faculty of Engineering: Alejandro García, Manuel Osio, Miguel Velasco, Esteban Hernández†, Janette Tovar, Hugo Hernández, and Samuel Esteves.

Conflicts of Interest: The authors declare no conflict of interest.

References

1. Trogu, A.; Rainiere, G.; Fischanger, F. 3D Electrical Resistivity Tomography to Improve the Knowledge of the subsoil below Existing Buildings. *Environ. Semeiot.* **2011**, *4*, 63–70. [CrossRef]
2. Santarato, G.R.; Occhi, G.; Morelli, M.; Fischanger, F.; Gualerzi, D. Three-dimensional Electrical Resistivity Tomography to control the injection of expanding resins for the treatment and stabilization of foundation soils. *Eng. Geol.* **2011**, *119*, 18–30. [CrossRef]
3. Tsokas, G.N.; Diamanti, N.; Tsourlos, P.I.; Vargemezis, G.; Stampolidis, A.; Raptis, K.T. Geophysical prospection at Hamza bey (Alkazar) monument, Thessaloniki, Greece. *Mediterr. Archaeol. Archaeom.* **2013**, *13*, 9–20.
4. Alfy, M.E.; Lashin, A.; Faraj, T.; Alataway, A.; Tarawneh, Q.; Al-Bassam, A. Quantitative hydro-geophysical analysis of a complex structural karst aquifer in Eastern Saudi Arabia. *Sci. Rep.* **2019**, *9*, 2825. [CrossRef]
5. Slater, L.; Binley, A.; Brown, D. Electrical Imaging of Fractures Using Ground-Water Salinity Change. *Ground Water* **1997**, *35*, 436–442. [CrossRef]
6. Sogade, J.A.; Scira-Scarppuzzo, F.; Vichabian, Y.; Shi, W.; Rodi, W.; Lesmes, D.P.; Morgan, F.D. Induced-polarization and mapping of contaminant plumes. *Geophysics* **2006**, *71*, 75–84. [CrossRef]
7. Binley, A.; Cassiani, G.; Middleton, R.; Winship, P. Vadose zone flow parameterization using cross-borehole radar and resistivity imaging. *J. Hydrol.* **2002**, *267*, 147–159. [CrossRef]
8. Ramirez, A.; Daily, W.; LaBrecque, D.; Owen, E.; Chestnut, D. Monitoring an underground steam injection process using electrical resistance tomography. *Water Resour.* **1993**, *29*, 73–87. [CrossRef]
9. LaBrecque, D.J.; Morelli, G.; Daily, W.; Ramirez, A.; Lundegard, P. Occam's inversion of 3-D electrical resistivity tomography. In *Three-Dimensional Electromagnetics*; Spies, B., Ed.; Society of Exploration Geophysicists: Tulsa, OK, USA, 1999; pp. 575–590.
10. Newmark, R.; Aines, R.; Hudson, G.; Lif, R.; Chiarappa, M.; Carrigan, C.; Nitao, J.; Elsholz, A.; Eaker, C. An integrated approach to monitoring a field test of in situ contaminant destruction. In *Symposium on the Application of Geophysics to Engineering and Environmental Problems*; Environmental & Engineering Geophysical Society: Bloomfield, CT, USA, 1999; pp. 527–539. [CrossRef]
11. Allred, B.; Reza, E.M.; Saraswat, D. Comparison of electromagnetic induction, capacitively-coupled resistivity, and galvanic contact resistivity methods for soil electrical conductivity measurement. *Appl. Eng. Agric.* **2006**, *22*, 215–230. [CrossRef]
12. Sabrina, B. Searching for graves using geophysical technology: Field Tests with ground penetrating radar, magnetometry, and electrical resistivity. *J. Forensic Sci.* **2003**, *48*, 5–11.
13. Jervis, R.; Pringle, J.K.; Tuckwell, G.W. Time-lapse resistivity surveys over simulated clandestine graves. *Forensic Sci. Int.* **2009**, *192*, 7–13. [CrossRef]
14. Gough, D.O.; Sekii, T. On the effect of error correlation on linear inversions. *Mon. Not. R. Astron. Soc.* **2002**, *335*, 170–176. [CrossRef]
15. LaBrecque, D.; Daily, W.; Adkins, P. Systematic errors in resistivity measurement systems. In Proceedings of the 20th EEGS Symposium on the Application of Geophysics to Engineering and Environmental Problems, Denver, CO, USA, 1–5 April 2007. [CrossRef]
16. Dahlin, T.; Leroux, V.; Nissen, J. Measuring techniques in induced polarization imaging. *J. Appl. Geophys.* **2002**, *50*, 279–298. [CrossRef]
17. Rossi, M.; Dahlin, T.; Olsson, P.I.; Günther, T. Data acquisition, processing and filtering for reliable 3D resistivity and time-domain induced polarization tomography in an urban area: Field example of Vinsta, Stockholm. *Near Surf. Geophys.* **2018**, *16*, 220–229. [CrossRef]
18. Fiandaca, G.; Auken, E.; Christiansen, A.V.; Gazoty, A. Time domain induced polarization: Full-decay forward modelling and 1D laterally constrained inversion of Cole-Cole parameters. *Geophysics* **2012**, *77*, E213–E225. [CrossRef]
19. Sheriff, R.E. *Encyclopedic Dictionary of Applied Geophysics*, 4th ed.; Society of Exploration Geophysicists: Tulsa, OK, USA, 2002; ISBN 978-1-56080-118-4. [CrossRef]
20. Davydycheva, S.; Rykhlinski, N.; Legeido, P. Electrical-prospecting method for hydrocarbon search using the induced-polarization effect. *Geophysics* **2006**, *71*, G179–G189. [CrossRef]
21. López-González, A.E.; Tejero-Andrade, A.; Hernández-Martínez, J.L.; Prado, B.; Chávez, R.E. Induced Polarization and Resistivity of Second Potential Differences (SDP) with Focused Sources Applied to Environmental Problems. *J. Environ. Eng. Geophys.* **2019**, *24*, 49–61. [CrossRef]
22. Lei, Z.; Tianqi, G.; Ji, Z.; Shijun, J.; Qingzhou, S.; Ming, H. An adaptive moving least squares method for curve fitting. *Measurement* **2014**, *49*, 107–112. [CrossRef]
23. Iris Instruments. Processing Software. Available online: https://www.iris-instruments.com/syscal-prosw.html (accessed on 11 May 2024).
24. Baba, K.; Bahi, L.; Ouadif, L. Enhancing geophysical signals through the use of Savitzky-Golay filtering method. *Geofísica Int.* **2014**, *53*, 399–409. [CrossRef]
25. Bakkali, S. Using Savitzky-Golay filtering method to optimize surface phosphate deposit disturbances. *Ingenierías* **2007**, *10*, 399–409.

26. Ritz, M.; Robain, H.; Pervago, E.; Albouy, Y.; Camerlynck, C.; Descloitres, M.; Mariko, A. Improvement to resistivity pseudosection modelling by removal of near-surface inhomogeneity effects: Application to a soil system in south Cameroon. *Geophys. Prospect.* **1999**, *47*, 85–101. [CrossRef]
27. Flores, A.; Kemna, A.; Zimmermann, E. Data error quantification in spectral induced polarization imaging. *Geophysics* **2012**, *77*, 227–237.
28. Chandrasekhar, E.; Eswara Rao, V. Wavelet Analysis of Geophysical Well-log Data of Bombay Offshore Basin, India. *Math. Geosci.* **2012**, *44*, 901–928. [CrossRef]
29. Li, J.; Zhanxiang, H.; Liu, Q.H. Higher-order statistics correlation stacking for DC electrical data in the wavelet domain. *J. Appl. Geophys.* **2013**, *99*, 51–59. [CrossRef]
30. Deo, R.N.; Cull, J.P. Denoising time-domain induced polarization data using wavelet techniques. *Explor. Geophys.* **2016**, *47*, 108–114. [CrossRef]
31. Paine, J.; Copeland, A. Reduction of noise in induced polarization data using full time-series data. *Explor. Geophys.* **2003**, *34*, 225–228. [CrossRef]
32. Fox, R.C.; Hohmann, G.W.; Killpack, T.J.; Rijo, L. Topographic effects in resistivity and induced polarization surveys. *Geophysics* **1980**, *45*, 75–93. [CrossRef]
33. Oldenburg, D.; Li, Y. Inversion of induced polarization data. *Geophysics* **1994**, *59*, 1327–1341. [CrossRef]
34. Savitzky, A.; Golay, M.J.E. Smoothing and differentiations of data by simplified least squares procedures. *Anal. Chem.* **1964**, *36*, 1627–1639. [CrossRef]
35. Haykin, S. *Adaptive Filter Theory*, 4th ed.; Prentice-Hall: Upper Saddle River, NJ, USA, 2002.
36. Zhou, B.; Dahlin, T. Properties and effects of measurement error on 2D resistivity imaging surveying. *Near Surf. Geophys.* **2003**, *1*, 105–117. [CrossRef]
37. Oldenborger, G.; Routh, P.; Knoll, M. Sensitivity of electrical resistivity tomography data to electrode position errors. *Geophys. J. Int.* **2005**, *163*, 1–9. [CrossRef]
38. Pazzi, V.; Ceccatelli, M.; Ciani, L.; Patrizi, G.; Guidi, G.; Cappuccini, L.; Casagli, N.; Catelani, M. Analysis of the Influence of the GPS Errors Occurred While Collecting Electrode Coordinates on the Electrical Resistivity of Tumuli. *Sensors* **2020**, *20*, 2966. [CrossRef] [PubMed]
39. Mexican Geological Service 2002. Geological-Mining Chart. México City E14-2. *Scale 1:250000. First Edition*. Available online: https://www.sgm.gob.mx/CartasPdf/GeologicasL.jsp (accessed on 2 February 2025).

Disclaimer/Publisher's Note: The statements, opinions and data contained in all publications are solely those of the individual author(s) and contributor(s) and not of MDPI and/or the editor(s). MDPI and/or the editor(s) disclaim responsibility for any injury to people or property resulting from any ideas, methods, instructions or products referred to in the content.